

Novel multimodality segmentation using level sets and Jensen-Rényi divergence

Daniel Marke^{a)}

Medical Physics Unit, University of McGill, Montreal, Quebec H3H 2R9, Canada

Habib Zaidi

Division of Nuclear Medicine and Molecular Imaging, Geneva University Hospital, CH-1211 Geneva, Switzerland; Geneva Neuroscience Center, Geneva University, CH-1205 Geneva, Switzerland; and Department of Nuclear Medicine and Molecular Imaging, University of Groningen, University Medical Center Groningen, Groningen P.O. Box 30 001, The Netherlands

Issam El Naqa

Faculty of Medicine, Department of Oncology, Medical Physics Unit, McGill University, Montreal, Quebec H3G 1A4, Canada

(Received 21 May 2013; revised 11 October 2013; accepted for publication 15 October 2013; published 14 November 2013)

Purpose: Positron emission tomography (PET) is playing an increasing role in radiotherapy treatment planning. However, despite progress, robust algorithms for PET and multimodal image segmentation are still lacking, especially if the algorithm were extended to image-guided and adaptive radiotherapy (IGART). This work presents a novel multimodality segmentation algorithm using the Jensen-Rényi divergence (JRD) to evolve the geometric level set contour. The algorithm offers improved noise tolerance which is particularly applicable to segmentation of regions found in PET and cone-beam computed tomography.

Methods: A steepest gradient ascent optimization method is used in conjunction with the JRD and a level set active contour to iteratively evolve a contour to partition an image based on statistical divergence of the intensity histograms. The algorithm is evaluated using PET scans of pharyngolaryngeal squamous cell carcinoma with the corresponding histological reference. The multimodality extension of the algorithm is evaluated using 22 PET/CT scans of patients with lung carcinoma and a physical phantom scanned under varying image quality conditions.

Results: The average concordance index (CI) of the JRD segmentation of the PET images was 0.56 with an average classification error of 65%. The segmentation of the lung carcinoma images had a maximum diameter relative error of 63%, 19.5%, and 14.8% when using CT, PET, and combined PET/CT images, respectively. The estimated maximal diameters of the gross tumor volume (GTV) showed a high correlation with the macroscopically determined maximal diameters, with a R^2 value of 0.85 and 0.88 using the PET and PET/CT images, respectively. Results from the physical phantom show that the JRD is more robust to image noise compared to mutual information and region growing.

Conclusions: The JRD has shown improved noise tolerance compared to mutual information for the purpose of PET image segmentation. Presented is a flexible framework for multimodal image segmentation that can incorporate a large number of inputs efficiently for IGART. © 2013 American Association of Physicists in Medicine. [<http://dx.doi.org/10.1118/1.4828836>]

Key words: statistical divergence measures, multimodal segmentation, PET/CT, level sets, clinical oncology

1. INTRODUCTION

Radiotherapy is an important modality for treating patients with cancer. About 60%–70% of all cancer patients receive irradiation as part of their treatment¹ and this remains the main option for advanced stages of disease. However, geometric and dosimetric uncertainties during fractionated radiotherapy can accumulate daily from tumor regression, soft-tissue deformations, and organ motion. Traditionally, computed tomography (CT) has been the principal modality used for radiotherapy treatment planning. However, several studies have shown inter- and intraobserver variability in manual gross tu-

mor volume (GTV) delineation as high as 700% (Refs. 2–4) and 80% (Ref. 5) using CT alone, respectively. The inclusion of positron emission tomography (PET) into the treatment planning process has provided improved contrast and increased sensitivity to metabolically active regions of the tumor versus normal background tissue. However, PET suffers from relatively low spatial resolution, variable uptake patterns, and quantum image noise. These properties can drastically influence the intended treatment target.

Even assuming perfect initial target definition, a patient's anatomy as well as the target itself may change drastically during the course of treatment. Tumor regression in the lung

on the order of 1.2% of the volume per day was observed in a study by Kupelian *et al.*⁶ using megavoltage CT images. In a study by Barker *et al.*, an average volume change of 1.8% per day was observed in the head and neck.⁷ In the same study, average weight loss of 7.1% of the body mass was observed over the course of treatment. The feasibility of image-guided adaptive radiotherapy (IGART) relies on fast and accurate algorithms that can reduce treatment planning time.⁸ Often cone-beam computed tomography (CBCT) or megavoltage computed tomography (MVCT) is used to check the anatomical context of the patient. These modalities tend to suffer from a reduction in contrast and increase in image noise, thus making it difficult to redefine the target boundary accurately.

A large number of automated and semiautomated methods have emerged in the literature attempting to provide consistent interpretation of the tumor boundary. These have included a large number of soft threshold values ranging within 15%–50% of the maximum standardized uptake value (SUV),^{9–13} and a hard value of 2.5 SUV.¹⁴ Further work has produced regression formulas to predict the most appropriate threshold value based on either mean SUV,¹⁵ lesion volume,¹⁶ or signal to background ratio (SBR).¹⁷ However, a few studies have noted that no appropriate threshold value exists that consistently and accurately determines the GTV boundary.^{16,18} This is partially due to inconsistent FDG-PET uptake from patient to patient as well as heterogeneous uptake patterns that are often seen within the tumor regions themselves. More advanced methods such as those using fuzzy hidden Markov chains¹⁹ or Markov random fields²⁰ have been proposed which make use of stochastic modelling to fit gaussian functions to the intensity distributions, using each voxel's class probability and agreement with surrounding voxels to randomly shuffle it around into other data classes. This process eventually converges, and finally classifies the voxels in the image into a number of hard classes. The information from surrounding voxels is often used to reduce errors produced by image noise. More recently, clustering methods have been receiving considerable attention due to the fact that they are able to approximate the intensity distributions of the segment and background without any knowledge about the shape of the distributions.^{21–23} Another popular method that has often seen commercial implementation is the atlas-based approach that uses the coregistration of a large database of patient scans to produce a probabilistic map of expected uptake values for healthy patients and then uses deviations from this map to determine where abnormal regions lie.^{24,25} While there has been a plethora of work regarding proper PET segmentation, the problem remains a challenging one that has not been satisfactorily resolved using single modality methods. A more thorough review of PET segmentation algorithms can be found in surveys by Zaidi and El Naqa²⁶ and Sheperd *et al.*²⁷

We have adapted an active contour approach due to its ability to define the contour using a continuous function which can intuitively adapt to topological changes such as splitting and merging of multiple regions, as encountered in a heterogeneous tumor and to achieve subpixel accuracy. Ac-

tive contours are a class of methods by which an initialized segment is evolved over time to maximize a chosen energy function. Internal forces specific to the shape of the contour along with external forces from the image itself are both used in this evolutionary process which follows the gradient field of the function. The active contour can be defined explicitly as is the case with snakes²⁸ where the contour is given by the positions of a set of points, or implicitly as with level sets,^{29,30} where it is represented by the zero level of a scalar function.

Another important facet of our work regards the consideration of complementary information from different modalities to delineate the so-called “biophysical” target.³⁰ A study by Milker-Zabel *et al.*³¹ showed that with the inclusion of PET, CT, and MRI modalities into the treatment planning process for stereotactic radiotherapy resulted in changes to the target definitions 73% of the time. The challenge with multimodality treatment planning stems from registering patient images that often do not include a high degree of correlating details. The inclusion of hybrid PET/CT imaging devices over the past ten years has greatly aided in reducing interobserver variability in target definition^{32,33} by providing physically registered datasets. The interpretation of visual information from multiple images is another source of variability that may be aided by computer automation. A number of algorithms addressing the issue of multimodality segmentation, particularly with regards to PET/CT segmentation have been recently published.^{30,34–37} These include a simple region growing method where the user places a seed within the area to be segmented which then begins to absorb surrounding voxels that fall within a given intensity range, growing until it fills the entire connected region. This method has been applied in the context of the lung³⁴ using PET/CT images but found to produce systematic overestimation of the tumor boundary. Probabilistic classification using a number of textural filters and machine learning techniques trained on a set of previously observed cases has been shown to produce accurate results in the head and neck area.³⁵ Within the same area of the body, a semiautomated graph-based method has been tested that uses Markov Random Fields to produce globally optimal solutions.³⁶ Within our own group, we have applied an active contour to the task of PET/CT segmentation with the development of the multivalued level sets segmentation method.³⁰ This method employed an energy metric based on differences between voxel intensity and the mean intensity values found inside and outside the segment. This approach however, does not account for the spread and shape of individual image intensity distribution reducing each to a single weighting parameter in the algorithm.

The Jensen-Rényi divergence (JRD) is a relatively new generalized information divergence measure whose curvature can change based on a chosen parameter (α). Our implementation relies on a nonparametric approach that makes no assumptions about the underlying distribution. Some studies have observed that the JRD is more robust to image noise than mutual information when applied to registration as long as the weighting parameters are chosen appropriately.^{38,39} Mutual information is a common objective function for

registration tasks, and while it is not commonly used for segmentation, it is based on entropy terms which a number of authors have investigated for use in segmentation.^{40–43} The use of entropy based on intensity value histograms (in particular using nonparametric density estimates) is an effective objective for statistically based segmentation. Using the metric, it is possible partition regions with subtle differences in their intensity distribution that may be too difficult to detect with simple average intensity methods or the naked eye. Mutual information also has a similar mathematical formulation to the JRD and hence is used for comparison in this paper. To date the JRD has not been applied as a metric for segmentation using a level set active contour framework. The goals of this work are threefold. First, we show that the JRD can improve noise tolerance when applied to the task of segmentation using PET and CT scans of an inhouse phantom. Second, we evaluate the JRD based level sets method with regards to PET segmentation using PET scans of patients with pharyngolaryngeal squamous cell carcinoma. Third, we demonstrate its application to segmentation of multimodality PET/CT scans of patients with lung carcinoma.

2. MATERIALS AND METHODS

The implementation and validation of the proposed method is developed in this section starting with a theoretical background of the energy term used in level sets method. Here we present the derived solution to the level sets differential equation using the JRD. The materials and methods for collecting the validation data along with an explanation of the validation metrics is then provided followed by hardware and software specifications of our implementation.

2.A. Theory

2.A.1. Level sets

A level set function $\phi(u, v, w)$ is used to implicitly define a contour within our image, where $x = (u, v, w)$ defines a set of 3D cartesian coordinates within the image volume. ϕ is a scalar function that defines the contour edge by its zero level ($\phi(u, v, w) = 0$).

Let E be a function of a level set. The successive iterations of the minimization/maximization of E using a steepest descent/ascent approach corresponds to a specific evolution of the level set, and hence of its zero level

$$E(\phi) = \int_{\Omega} (\text{JRD}(\phi(x)) + \mu |\nabla H(\phi(x))| - \nu) dx, \quad (1)$$

where $\text{JRD}(\phi)$ is the Jensen Rényi divergence, ν is a scalar velocity term, dx is an infinitesimally small volume at point x (which is defined by the image resolution), Ω is the set of sampled voxels in the image, $|\nabla H(\phi)|$ is the magnitude of the gradient of the Heaviside function (which forces a smooth boundary) and is defined by Eq. (3), μ is a weighting factor. Following curve evolution theory, evolving the energy function over time is equivalent to finding the

derivative over the contour

$$\frac{\partial \phi}{\partial t} = \frac{\partial E(C)}{\partial C}, \quad (2)$$

where C is the contour at the current iteration defined by the zero level ($\phi(C) = 0$) of the level set function

$$H(\phi) = \begin{cases} 1, & \text{if } \phi \geq 0 \\ 0, & \text{else.} \end{cases} \quad (3)$$

2.A.2. The Jensen Rényi divergence

For estimation of the JRD, we start by defining a set of samples from either outside or inside a contour by $x_i, i = 1, 2, \dots, n$ where n is the sample size and i is the sample index. If we let $P = (P(J(x_1), \Omega), P(J(x_2), \Omega), \dots, P(J(x_n), \Omega))$ be the probability density distribution, where $J(x_i)$ is the intensity value of sample x_i , then we can define the Jensen Renyi entropy using Eq. (4),

$$R_{\alpha}(P) = \frac{1}{1 - \alpha} \log \sum_{i=1}^k P(J(x_i), \Omega)^{\alpha}, \quad (4)$$

where $J(x)$ is the feature vector at point x made up of the intensity values of the input images and α defines the curvature of the function. For $\alpha \in (0, 1)$ the function is concave, whereas it is neither convex nor concave for $\alpha > 1$. Choosing an α value of 1 gives back the Shannon entropy. The JRD criterion is defined by the following conditional expectation:

$$\begin{aligned} E(\phi) &= \text{JRD}(\phi) \\ &= R_{\alpha} \left(\sum_{k=1}^n w_k P_k \right) - \sum_{k=1}^n w_k R_{\alpha}(P_k) \\ &= \frac{1}{1 - \alpha} \left[\log \int_{\mathfrak{R}} (w_1 P_1(J, \Omega_-) + w_2 P_2(J, \Omega_+))^{\alpha} dJ \right. \\ &\quad \left. - w_1 \log \int_{\mathfrak{R}} (P_1(J, \Omega_-))^{\alpha} dJ \right. \\ &\quad \left. - w_2 \log \int_{\mathfrak{R}} (P_2(J, \Omega_+))^{\alpha} dJ \right], \quad (5) \end{aligned}$$

where w_1, w_2 are the weighting parameters for the probability distribution functions P_1 and P_2 . P_1 and P_2 in this context are defined by the intensity distributions inside and outside the evolving level set, respectively. \mathfrak{R} is the domain of feature values represented by J . The set of samples defining these regions is referred to by Ω_- for inside the segment and Ω_+ for outside the segment.

The divergence measure changes with the parameter α . For example, when alpha is equal to 0.5, the divergence is proportional to the log of the Bhattacharyya coefficient. When α is chosen to be 1, Renyi entropy reduces to the Shannon entropy [SE in Eq. (6)] and the measure becomes the Jensen-Shannon divergence. This becomes equivalent to mutual information when the weighting parameters w_1 and w_2 are chosen equal to $P_1(J, \Omega_-)$ and $P_2(J, \Omega_+)$ for each sample.³⁸ The weighting parameters determine the importance of probability

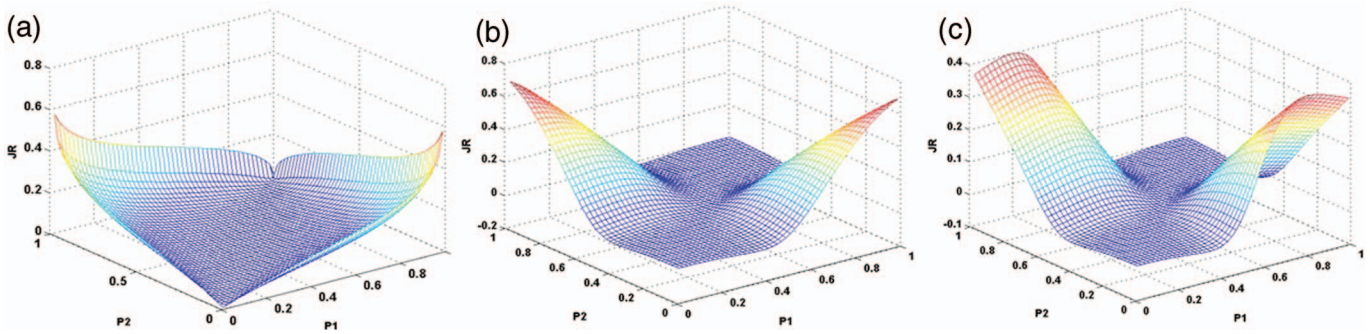


FIG. 1. Mesh plots of the JRD energy space using Bernoulli distributions for P_1 and P_2 . In this context $P_k = (p_k, 1 - p_k)$ replaces $P(J(x_i), \Omega)$ in Eqs. (4) and (6). In (a) alpha is chosen equal to 1 with equal weights. (b) shows the function with $\alpha = 5$, $w_1 = 0.75$, and $w_2 = 0.25$. The segmentation algorithm would maximize the JRD, these are the spots in the energy space where there is the largest difference between P_1 and P_2 if the weighting values are equal. Changing the weighting parameters affects where these maxima occur.

distributions P_1 and P_2 which in this case represents the foreground and background. For this work, the weighting parameters were chosen to be 0.5 each. On a continuous basis, α can be seen to change the curvature of the divergence measure as shown in Fig. 1. Here \mathfrak{R} covers the domain of possible intensity values. For our implementation, volumes were discretized to 40 levels in order to reduce processing time requirements

$$SE(P) = \sum_{i=1}^n P(J(x_i), \Omega) \log(P(J(x_i), \Omega)). \quad (6)$$

The probability distribution functions are defined as follows:

$$P(J, \Omega) = \frac{1}{n} \sum_{i=1}^n K_{\psi}(J - J(x_i)), \quad (7)$$

where

$$\begin{aligned} K_{\psi}(J - J(x_i)) &= (2\pi)^{-t/2} |\psi|^{-1/2} \\ &\times \exp\left(-\frac{1}{2}(J - J(x_i))^T \psi^{-1}(J - J(x_i))\right), \end{aligned} \quad (8)$$

where K_{ψ} is the Gaussian kernel used for the Parzen window estimation of the probability density.⁴⁴ Here ψ represents the covariance matrix of the feature vector J . This can be calculated directly from the vector J , however this makes the assumption that the data are best represented by two unimodal distributions. Since we want to make no assumptions about the shape of the distributions, every covariance matrix was set to a $t \times t$ matrix with every diagonal element equal to 8. Here t is the dimensionality of the feature vector J ,

$$\begin{aligned} \frac{\partial \phi}{\partial t} &= \delta(\phi) \left(\left(\frac{\nabla \phi}{|\nabla \phi|} \right) \right. \\ &+ \frac{1}{1 - \alpha} \frac{\int_{\mathfrak{R}} \alpha (w_1 P_1(J, \Omega_-) + w_2 P_2(J, \Omega_+))^{\alpha-1} (w_1 \frac{\partial P_1}{\partial C} + w_2 \frac{\partial P_2}{\partial C}) dJ}{\int_{\mathfrak{R}} (w_1 P_1(J, \Omega_-) + w_2 P_2(J, \Omega_+))^{\alpha} dJ} \\ &- \frac{1}{1 - \alpha} w_1 \frac{\int_{\mathfrak{R}} \alpha P_1(J, \Omega_-)^{\alpha-1} \frac{\partial P_1}{\partial C} dJ}{\int_{\mathfrak{R}} P_1(J, \Omega_-)^{\alpha} dJ} \\ &\left. - \frac{1}{1 - \alpha} w_2 \frac{\int_{\mathfrak{R}} \alpha P_2(J, \Omega_+)^{\alpha-1} \frac{\partial P_2}{\partial C} dJ}{\int_{\mathfrak{R}} P_2(J, \Omega_+)^{\alpha} dJ} - \nu \right), \end{aligned} \quad (9)$$

where $\delta(\phi)$ is approximated by the following:

$$\delta(\phi) = \frac{1}{\pi \epsilon (1 + (\phi/\epsilon)^2)}, \quad (10)$$

where ϵ is a small number arbitrarily chosen to be 10^{-7} . The partial derivatives of the probability densities are

$$\begin{aligned} \frac{\partial P_1}{\partial C} &= \frac{\partial P_1(J, \Omega_-)}{\partial C} \\ &= \frac{1}{|\Omega_-|} (-K_{\psi_1}(J(C) - J) - P_1(J, \Omega_-)), \end{aligned} \quad (11)$$

$$\begin{aligned} \frac{\partial P_2}{\partial C} &= \frac{\partial P_2(J, \Omega_+)}{\partial C} \\ &= \frac{1}{|\Omega_+|} (P_2(J, \Omega_+) - K_{\psi_2}(J(C) - J)). \end{aligned} \quad (12)$$

When using p multiple inputs, or in our case multiple images, the vector of intensity values, J simply becomes a $p \times n$ vector where each data point is sampled from the same spatial location in the domain of the images. A maximum sample size of 1600 voxels or the total number of voxels in a sample

region (whichever is smaller) is used to estimate the probability distribution functions for inside and outside the segment. The samples are randomly taken from the inside of the segment and an equally sized area surrounding it which is created using a distance transform of the contour edge and masking the values within the appropriate distance. The integrals in Eq. (9) can be further simplified if α is chosen to be an integer greater than 1. We encourage the reader to check the Appendix for further details regarding this simplification, which leads to a reduction in processing time.

Unless stated otherwise, the following parameters, ($\nu = 0$, $\alpha = 2.5$, $\mu = 0.11$), were used during segmentation of PET/CT and PET alone and ($\nu = 0$, $\alpha = 0.85$, $\mu = 0.11$) for CT alone.

2.B. Datasets and validation

2.B.1. Experimental phantom studies

A physical phantom was constructed in order to evaluate the performance of the algorithm under varying conditions of image quality. This was done by placing a small glass jar with a 64 mm inner diameter with 4 mm thick walls wrapped in a 3 mm thick bolus sheet inside a larger glass jar with an outer diameter of 111 and 7 mm thick walls which is shown in Fig. 2. Thread seal tape was used to make the larger jar water tight. The phantom was filled with a solution of approximately 950 ml of water with 8.7875 MBq of ^{18}F -FDG radiotracer for a concentration of 9250 Bq/ml. The inner jar is not sealed allowing the solution to mix inside the phantom producing a 1:1 concentration between the inside and outside of the inner jar. The purpose of this phantom was to have the semiautomated algorithm attempt to segment the boundary of the inner jar without spilling into the surrounding region. The phantom was scanned using a GE Discovery-ST PET/CT scanner (GE Healthcare) and reconstructed into a series of 128×128 voxel images with a resolution of 5.4688 mm in the transverse plane and a slice thickness of 3.27 mm using the ordered subset expectation maximization (OSEM) algorithm.

In order to achieve a variety of SNR values, 6 scan times of 4, 6, 9, 15, 62, and 246 s were chosen to produce 6 volumes. The measured SNRs from these scans were 9.1, 9.2, 10.9, 12.6, 17.8, and 26.0 dB using the definition of SNR given by Eq. (13). Where μ_{sig} and σ_{bkg} are the mean and stan-

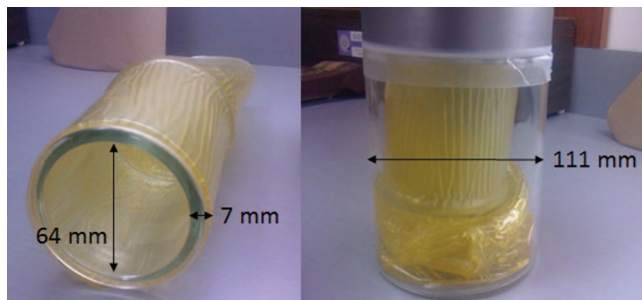


FIG. 2. The inner jar wrapped in the bolus sheet (left) and the two containers, one inside the other (right).

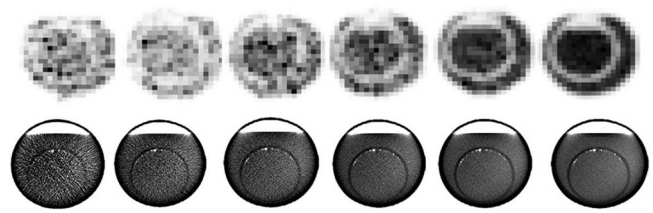


FIG. 3. Transverse slices of phantom PET scan for scan times of 4, 6, 9, 15, 62, and 246 s (from left to right in the top row). Slices of the phantom taken with the CBCT are shown in the bottom row with increasing SNR from left to right.

dard deviation of the signal and background. The signal in this case is the water within the inner jar since it contained the FDG where as the wall of the inner jar and the bolus emitted no signal and was thus considered background. Since the wall and the bolus occupied very little area, the region over the entire volume was used to provide a more accurate calculation of standard deviation. For the CT, μ_{sig} and σ_{bkg} are the mean and standard deviation of the intensity values found in the inner jar wall and using the inner region of water as the background. Transverse slices from these 6 scans are shown in Fig. 3.

$$\text{SNR} = 20 \cdot \log_{10} \left(\frac{\mu_{sig}}{\sigma_{bkg}} \right). \quad (13)$$

Similarly, the phantom was scanned using onboard cone beam computed tomography (CBCT). The images were all scanned using a voltage of 100 kV but with varying current and pulse width. CBCT scans were evaluated due to their poor contrast and low SNR. The applied scanning parameters along with the resulting SNRs are summarized in Table I.

Approximately 310 ml of Omnipaque 300 (65% iohexol, GE Healthcare Canada, Mississauga ON) was diluted in 640 ml of water for the CBCT scan and the bolus sheet removed. It was observed that the scan contained beam hardening artifacts and an asymmetric distribution of contrast agent. In order to correct for these heterogeneities, the regions of the phantom walls and the space in between were delineated with circles matching the dimensions of the phantom. A quasi-ideal version of the phantom was generated by uniformly filling these areas with the mean value found in the original scan. A third volume was generated using the voxel-by-voxel ratio of the quasi-ideal phantom to the original scan. This third volume was smoothed using a 3D bilateral filter and then used to rescale the phantom images to remove the inhomogeneity.

TABLE I. Scanning parameters for the CBCT.

Scan	current (mA)	Pulse width (ms)	SNR (dB)
1	10	10	25.3
2	20	10	29.2
3	40	10	31.8
4	40	20	33.9
5	80	20	35.3
6	80	32	35.7

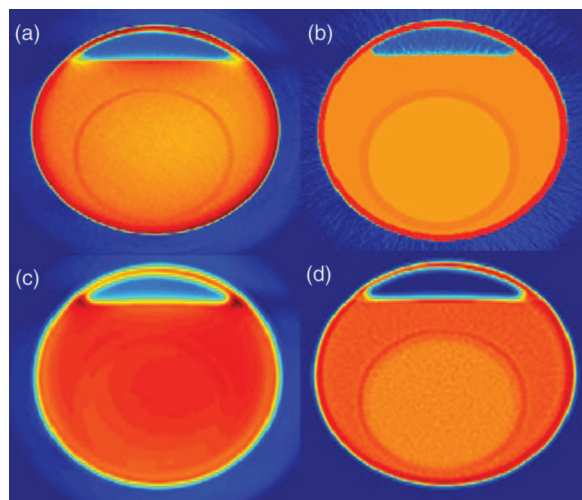


FIG. 4. Inhomogeneity correction with (a) the original CBCT slice (from scan #6). (b) The ideal phantom whose values are equal to the mean within the four regions found in (a). (c) The ratio of (b) to (a) following a bilateral filter smoothing, using $\sigma_1 = 13$, $\sigma_2 = 18$ and a tolerance of 0.02, and finally (d) the corrected image.

This is shown in Fig. 4. In order to compare the performance of the Jensen Rényi divergence versus using mutual information, two segmentation methods using an active contour but each driven by one of the two divergence measures was used to segment the region surrounded by the inner jar. Additionally, a region growing algorithm was also used to segment the inner jar for comparison. The region growing algorithm was given an intensity difference threshold of half the intensity difference between the water and jar wall values. This was found to produce favorable results in the highest SNR images for both modalities. This was done two-dimensionally over 19 slices from each volume for both PET and CBCT modalities. The performance of each method was measured by the average concordance index (CI) comparing the final segmentation to the known boundary of the inner jar.

2.C. Clinical studies

2.C.1. Louvain database

In addition to phantom studies, we included clinical validation datasets with a known reference from previous studies so that our results could easily be compared to other results reported in the literature.⁴⁵ PET scans of a subset of 7 patients with T-III to T-IV pharyngolaryngeal squamous cell carcinoma taken from the Louvain database were used for performance evaluation.⁴⁶ Patients were imaged on average five days prior to treatment which entailed a total laryngectomy. A 60 min dynamic 3D PET scan using an injection of 185–370 MBq of ^{18}F -FDG was performed on the selected patients, while immobilized with a thermoplastic mask. This was done with a ECAT EXACT HR camera (CTI Siemens, Knoxville, TN) and reconstructed using a 3D attenuation-weighted ordered subsets expectation minimization (AW-OSEM) algorithm into images of 128×128 voxels at a resolution of 2.1656×2.1656 mm in the transverse plane with a slice thickness of 3.125 mm. Following the laryngec-

tomy, resected tissue was placed in a polystyrene cast that was filled with a 16% gelatin solution and cooled to -20°C or 48 h and -80°C for a minimum of 72 h. Specimens were cut transversely into 1.7–2 mm slices that were then digitally scanned on both faces using a flatbed scanner. A reference segment of the perceived GTV was manually delineated using the digital scans of the macroscopic specimens and coregistered to the PET volume using a semiautomated rigid transformation using segmented structures as described by Daisne *et al.*⁴⁷

The PET images were segmented following a denoising procedure which consisted of smoothing using a bilateral 3D filter followed by deconvolution using the Landweber algorithm. For the JRD algorithm, segments were initialized using an anisotropic sphere that approximated the size of the GTV and ran for 100 iterations.

2.C.2. MAASTRO database

In order to evaluate the performance with regard to multimodal data, this study included a set of 33 patients with stage Ib-IIIb nonsmall cell lung carcinoma (NSCLC) treated at the Maastricht clinic in Maastricht, The Netherlands. Each has received a whole-body PET/CT scan using a Biograph SOMATOM Sensation 16 with an ECAT ACCEL PET scanner (Siemens, Erlangen, Germany). Patients were injected with an ^{18}F -FDG tracer following a 6 h fast. The dosage was determined using $(\text{weight} \times 4 + 20)$ MBq. A spiral CT with contrast was performed. The patient was then scanned in 5 min intervals covering 7 sections, beginning 45 min postinjection. The CT scan was used for attenuation correction and the PET data reconstructed using OSEM with eight subsets and four iterations. Of these 33 patients, 22 of which underwent surgical resection of the lung tumor, the maximal diameters of the tumor were measured macroscopically. This was used for comparison against the maximal tumor diameters produced by the JRD segmentation algorithm. The data collection is discussed in more detail in van Baardwijk *et al.*¹⁷

2.C.3. Validation metrics

With regards to the Louvain dataset, contours drawn from the images of the macroscopic specimens were used as a reference and validation was determined by two frequently used similarity metrics; CI and classification error (CE),

$$\text{CI} = \frac{A \cap B}{A \cup B}, \quad (14)$$

$$\text{CE} = \frac{\text{PCE} + \text{NCE}}{\text{Vol}} \times 100\%. \quad (15)$$

Here positive CEs (PCE) is the volume identified as background that is actually part of the tumor and negative CEs (NCE) is the volume identified as tumor that is actually background. *Vol* is the volume of the histologically derived contours. When defining CI, A, and B are defined as the segmented volume and macroscopically derived volume, respectively.

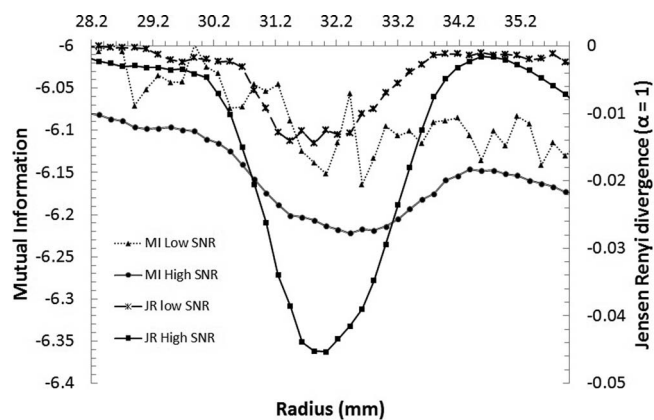


FIG. 5. JRD ($\alpha = 1$) and mutual information measured for circles of growing radius centered at the inner jar using the CBCT images. The low SNR scan had a SNR value of 32 and the high SNR scan had a value of 36. The peak is clearly preserved using the JRD when applied to the lower SNR image set.

The MAASTRO data were evaluated using the percent error of the maximal tumor diameter defined by Eq. (16),

$$\%error = \frac{|\max D_{seg} - \max D_{macro}|}{\max D_{macro}} \tag{16}$$

This was done due to the fact that the binary tumor masks were unavailable, only maximal tumor diameter was used in the original study.

2.C.4. Hardware and implementation

The JRD based level sets method was implemented in Matlab on a laptop with an Intel Core i7-2630QM @2GHz using 16GB of RAM and an NVIDIA GEFORCE GTX 560M with 3 GB of integrated RAM. Each iteration was calculated on the GPU requiring 0.2–0.4 s per iteration using a single modality and 0.4–0.6 s per iteration when using two modalities.

3. RESULTS

3.A. Phantom studies

Using a slice from each scan that showed the inner jar wall surrounded by the outer jar, binary masks of circles of radii varying from 29 to 36 mm were used to measure the mutual information and Jensen Rényi divergence. Figures 5 and 6 show the mutual information and Jensen Rényi divergence for the different radii using the CBCT and PET scans. The minima for both functions occurs at the wall of the inner jar. The profiles for both divergences are shown for the lowest SNR scan and the highest. The profiles show a distinct difference between the two scans, the minima of the mutual information becomes severely distorted by the decrease in image SNR. This is reflected in the performance of the two algorithms when measured using the average concordance index as shown in Figs. 8 and 9 when applied to the CBCT and PET modalities, respectively. The region growing method showed a drastic decrease in performance for both modalities as noise

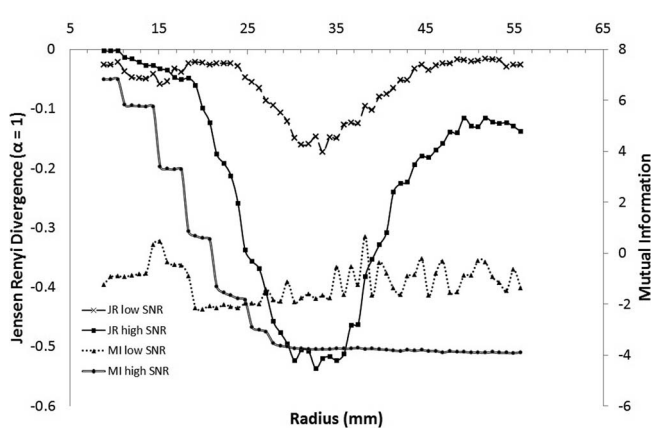


FIG. 6. JRD ($\alpha = 1$) and mutual information measured for circles of growing radius centered at the inner jar using the PET images. The low SNR scan had a SNR value of 9.2 and the high SNR scan had a value of 26.

in the image increase. Profiles of the JRD are affected by the choice of alpha value as shown in Fig. 7. Higher alpha values produce a sharper curve upon approaching the inner jar wall. The tails of the profiles are also increased with increasing alpha, these tails exist due to detection of the outer wall which lies partially adjacent to the bottom of the inner wall as shown in Fig. 4.

3.B. Clinical PET evaluation: Louvain database

The results from segmenting the PET images from the Louvain dataset are compared against those presented by Zaidi *et al.*,⁴⁵ where a comparison of nine algorithms is performed. The results are shown in terms of classification error and concordance index in Figs. 10 and 11. The JRD algorithm showed an average concordance index of 0.55 with a standard deviation of 0.12. This was second to the fuzzy clustering method incorporating spatial information and the \hat{a} trous wavelet transform (FCM-SW) which has a average CI of 0.59 with a somewhat smaller standard deviation of 0.08. Similar

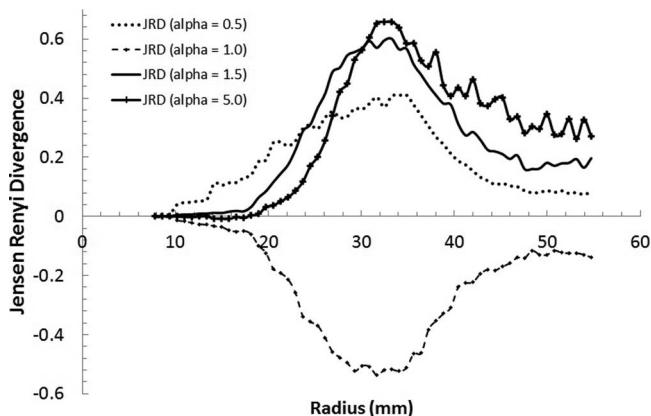


FIG. 7. The Jensen Rényi divergence measured for the PET scan of the noise phantom with circles of increasing radii. The profiles are shown with varying choices of parameter α . When α is equal to 1, the values become negative since the Rényi entropy reduces to the Shannon entropy as shown in Eq. (6).

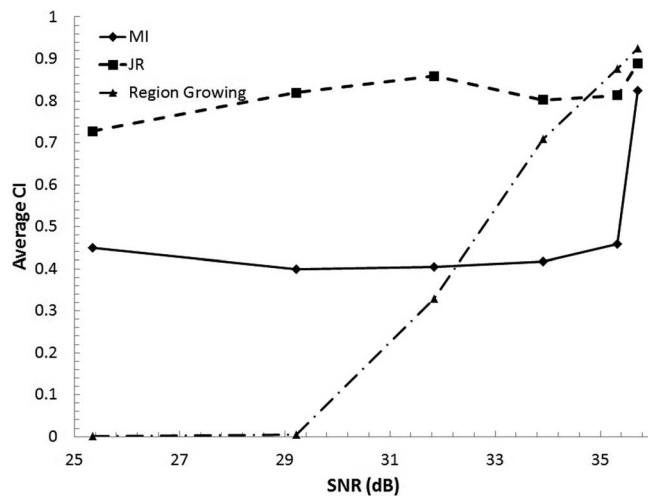


FIG. 8. The average concordance index of the active contour based on mutual information and the Jensen Rényi divergence for varying CBCT SNR values. The JRD shows a linear response to noise, whereas the mutual information shows a somewhat exponential decrease in performance.

results are reflected with regards to the average classification error where the JRD method had an average CE of 65% to 55% for the FCM-SW.

3.C. Clinical PET/CT evaluation: MAASTRO database

Figure 12 shows the percentage error of the maximum GTV diameter estimation for the JRD-based active contour when using PET, CT, and PET-CT together. The error is shown for each patient and shows a general trend of having the highest error when using CT alone and the lowest when using both modalities in conjunction. The correlation between maximal diameter estimate by the SBR method published by van Baardwijk *et al.* in 2007¹⁷ showed a R^2 value of 0.82. The same comparison using the results from the JRD based method using the PET image alone is shown in Fig. 13 and using the PET-CT together in Fig. 14. The estimated maximum diameter by the JRD method shows a higher correlation with the macroscopically determined diameter than the SBR technique when using only PET. This correlation is fur-

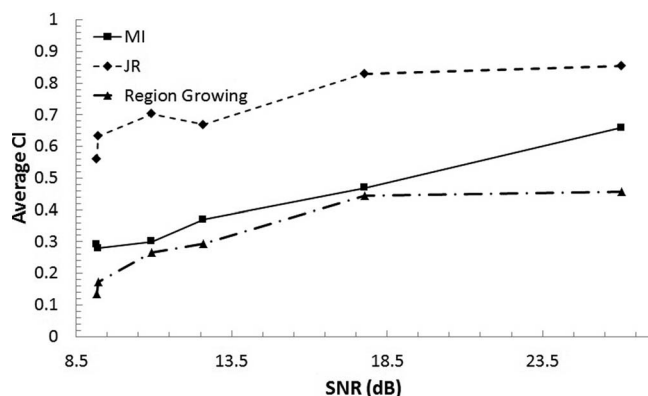


FIG. 9. The average concordance index of the active contour based on mutual information and the Jensen Rényi divergence for varying PET SNR values, controlled by the scan time.

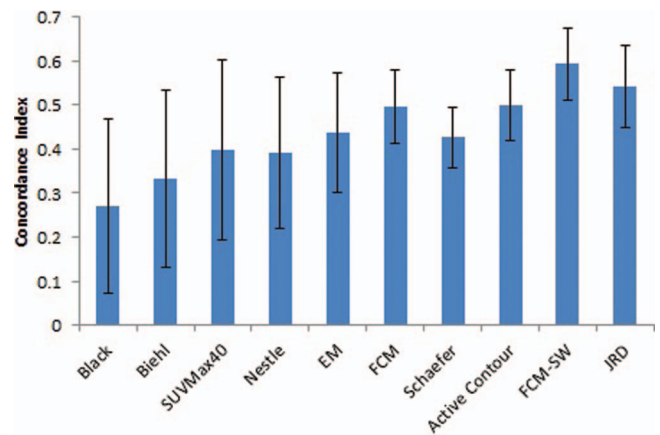


FIG. 10. The average concordance index of the JRD based active contour compared to nine other PET segmentation algorithms evaluated using the same data from Zaidi *et al.* (Ref. 45). Using only the PET intensity, the JRD based segmentation had an average CI of 0.55 versus 0.59 for the FCM-SW. The error bars represent one standard deviation.

ther improved when using the PET and CT information together which is not surprising considering the results shown in Fig. 12.

4. DISCUSSION

Hybrid imaging is becoming increasingly prevalent within radiotherapy clinics with the commercial introduction of PET/CT scanners over ten years ago and more recently with the advent of PET/MRI scanners. Consequently, radiation oncologists are required to consider multiple pieces of visual information when determining treatment targets yet the large majority of commercially available automated and semiautomated segmentation algorithms do not consider more than one modality at a time. Presented in this work is a novel multimodality segmentation algorithm based on the level set active contour method that relies on maximizing the Jensen Rényi divergence between the inside and outside domains of the

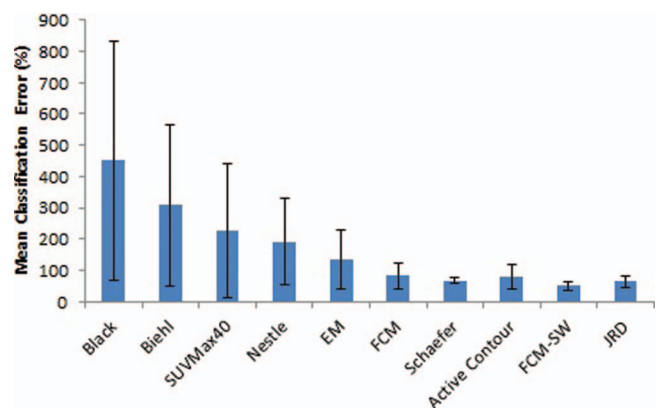


FIG. 11. The average classification error of the JRD based active contour compared to nine other PET segmentation algorithms evaluated using the same data from Zaidi *et al.* (Ref. 45). The JRD based segmentation had an average CE of 65% versus 50% for the FCM-SW. The error bars represent one standard deviation.

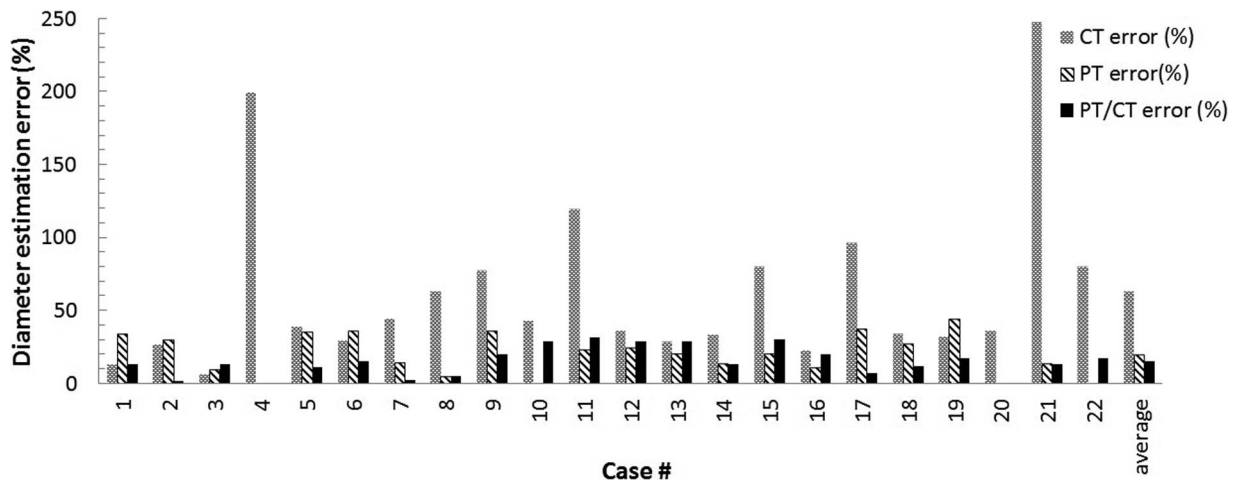


FIG. 12. The estimation error for the JRD based segmentation method of the GTV compared to the macroscopically determined maximum diameter. The average error was 63%, 19.5%, and 14.8% for the segmentations using CT only, PET only, and PET/CT. Particularly, high errors for cases 4 and 21 were seen when using CT alone due to the small size of the lesions and their proximity to the chest wall causing contour leakage.

contour. The advantage of using this divergence measure is twofold. The first is that when compared to mutual information, the JRD offers an improved robustness to sample variability and hence image noise. This is demonstrated using the phantom scans where not only is the difference in the energy space seen between the two measures, but the effect that this has on the performance for both PET and CT images is demonstrated in Figs. 8 and 9. The second advantage is that changing the alpha value can alter the energy space of the function and thus its tolerance to noise and the sensitivity of the final solution to subtle changes in intensity distribution.

The algorithm was tested using clinical single and multiple image modalities when performing segmentations. Considering the improved noise tolerance of the JRD and the fact that PET is a modality presenting with a large degree of inherent noise, it was appropriate to compare the segmentation method using PET alone versus other PET segmentation methods. This was done using the results from Zaidi *et al.*⁴⁵ that used data from the Louvain database. The JRD based method did not perform as well as the FCM-SW in regards to both average classification error and average concordance index (Figs. 10 and 11); however, this difference was not found to be statistically significant ($p = 0.52$ for CI and $p = 0.16$ for

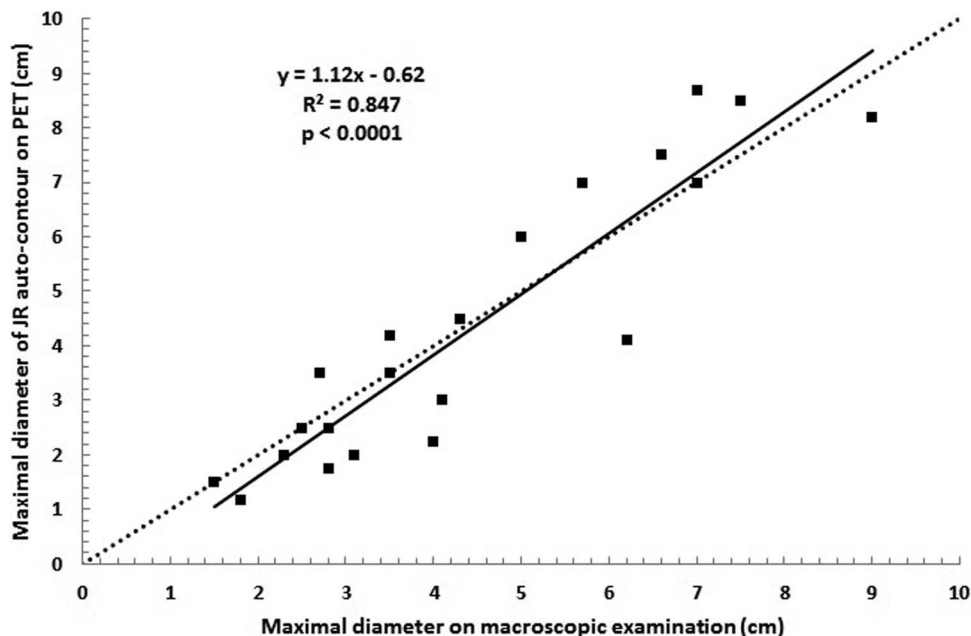


FIG. 13. The correlation of the JRD estimated maximum diameters versus the macroscopically determined maximum GTV diameters using only the PET image. The solid line shows the linear fit to the data, while the dotted line represents the ideal 1 to 1 linear relationship. The JRD based method shows a higher correlation compared to the SBR technique with a R^2 value of 0.85 versus 0.82.

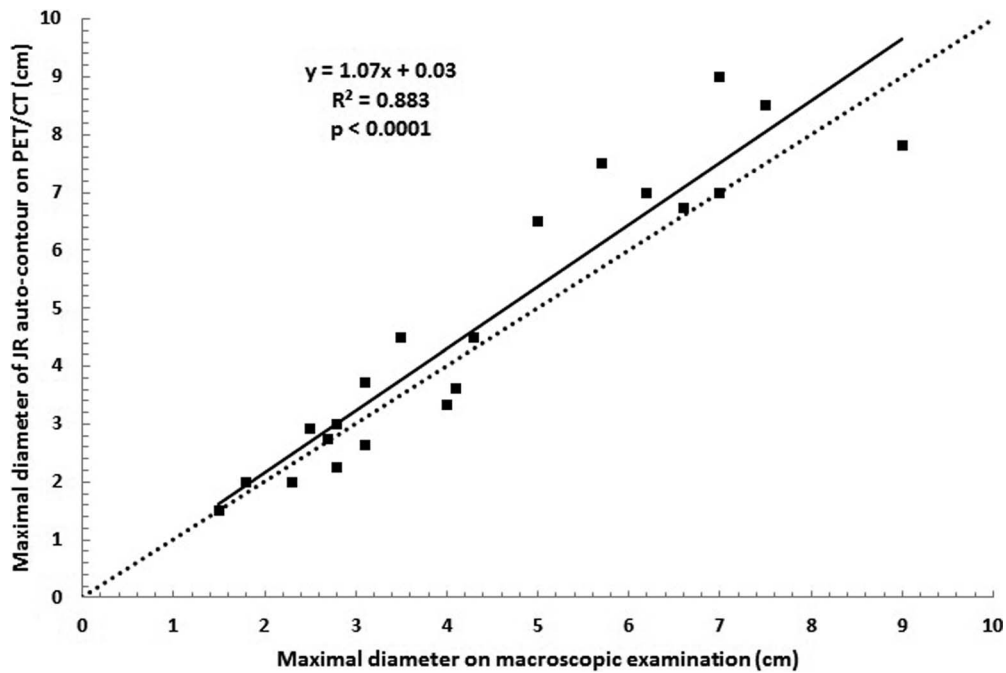


FIG. 14. The correlation of the JRD estimated maximum diameters versus the macroscopically determined maximum GTV diameters using both the PET and CT. The incorporation of both modalities shows an improved correlation versus using PET alone.

CE). It should also be noted that the FCM-SW algorithm utilizes both an anisotropic diffusion filter as well as the *à trous* wavelet transform as additional preprocessing steps, whereas the results for the JRD method as implemented incorporated only the PET intensity values. It may be possible to improve the JRD segmentation results by using the filters adopted by the FCM-SW algorithm since the JRD method can incorporate multiple inputs.

The MAASTRO data show that the JRD method can estimate maximum GTV diameter with a better correlation to the macroscopically determined diameters than using the SBR method which relies on fitting the most appropriate threshold to the lesion volume. The segmentation results show that using the PET information results in a higher accuracy than using the CT alone. This result has been observed previously^{4,35} and can be qualitatively seen on the contours shown in Figs. 15(c) and 15(d), where the CT contours had little contrast to follow when the GTV was connected to the mediastinum or chest wall. This led to leaking and over-estimation of the boundary which was the reason for the large errors seen for cases 4, 11, and 21 in the MAASTRO data shown in Fig. 12. By comparing the trends shown in Figs. 13 and 14, we see an increase in the adherence to a linear fit from the R-square value but also closer 1:1 linear relationship between the estimated maximum diameters using both PET and CT than with PET alone. This is seen from the slope of the trend lines. The combination of both PET and CT provides the most accurate segmentation, and the highest correlation to the reference, a result that has been previously observed.³⁵ Results from a 2011 study using the FCM-SW algorithm²³ to estimate maximum tumor diameter using the MAASTRO dataset showed a R-square value of 0.942, much

higher than using the JRD with either PET or PET/CT (see Figs. 13 and 14). The R-squared value of the FCM-S algorithm evaluated in the same study was only 0.81 emphasizing again the improvement made by including the *à trous* wavelet transform.

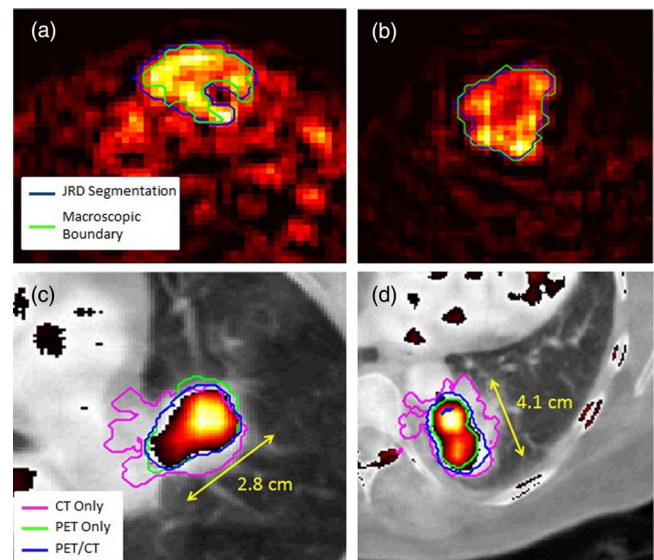


FIG. 15. A comparison of the JRD method applied to the Louvain (a) and (b) and MAASTRO (c) and (d) datasets with their respective references. In (a) and (b), the JRD method is shown compared to the macroscopically determined contour. For (c) and (d), the JRD method results are shown comparing the usage of CT alone, PET alone and PET/CT together with the maximum diameter of the GTV.

The JRD is a convenient objective function in that it can also be applied to the task of registration as investigated by a number of reports.^{38,39,48} This may facilitate future work involving the simultaneous segmentation and registration of multimodality images using this metric in order to reduce computation time and improve accuracy of both processes. Such an algorithm would have great application towards IGART where previous plan contours provide a good approximation for initialization.

5. CONCLUSIONS

This work has presented a novel multimodality segmentation algorithm using the Jensen-Rényi divergence with a level set contour. Using phantom CBCT and PET scans taken at various image quality levels, we demonstrate the improved noise robustness of the proposed objective compared to a traditional information-theoretic similarity measure (mutual information). The solution to the level set differential equation is presented along with clinical data validation using PET scans of 7 patients from the Louvain database with pharyngolaryngeal squamous cell carcinoma and 22 PET/CT scans from patients with lung carcinoma taken from the MAASTRO database. The JRD based approach has shown competitive performance compared to existing methods without much added pre- and postprocessing. More importantly, the approach allows for easy application to simultaneous multimodality segmentation as demonstrated in the phantom and clinical results.

ACKNOWLEDGMENTS

The authors would like to acknowledge Greg Tworck for his assistance in collecting the CBCT data and John Kildea for assisting with data collection. The authors also thank Dr. Dekker and Dr. De Ruyscher (MAASTRO clinic, Maastricht, The Netherlands) and Dr. Lee (Université Catholique de Louvain, Brussels, Belgium) for providing the clinical PET datasets. Funding was provided by the Natural Sciences and Engineering Research Council of Canada (NSERC-RGPIN 397711-11) and the Research Institute of the McGill University Health Centre. Dr. Zaidi is also supported by the Swiss National Science Foundation under Grant No. SNSF 31003A-135576 and Geneva Cancer League. The authors of this paper have no direct financial connection to the any commercial identities mentioned in the paper and no competing interests to disclose.

APPENDIX: ALGORITHM SIMPLIFICATION

The integrals of Eq. (9) can be simplified using the following property of convolution theory regarding the integral of

$$\partial\phi(x)/\partial C$$

$$= -\frac{2w_1^2(\hat{P}_{11} - P_{11}) + 2w_1w_2(P_{12} - \hat{P}_{12} + \hat{P}_{21} - P_{21}) + 2w_2^2(P_{22} - \hat{P}_{22})}{(w_1^2P_{11} + w_2w_2(P_{12} + P_{21}) + w_2^2P_{22})} + \frac{2w_1(\hat{P}_{11} - P_{11})}{P_{11}} + \frac{2w_2(P_{22} - \hat{P}_{22})}{P_{22}}. \quad (A5)$$

two Gaussian functions:

$$\begin{aligned} & \int g_p(x; a, A)g_p(x; b, B)dx \\ &= \int \frac{1}{(2\pi)^{p/2} |A|^{1/2}} e^{-\frac{1}{2}(x-a)'A^{-1}(x-a)} \\ & \quad \times \frac{1}{(2\pi)^{p/2} |B|^{1/2}} e^{-\frac{1}{2}(x-b)'B^{-1}(x-b)} dx \\ &= \frac{1}{(2\pi)^{p/2} |A+B|^{1/2}} e^{-\frac{1}{2}(a-b)'(A+B)^{-1}(a-b)}, \end{aligned} \quad (A1)$$

where a and b are offsets, or other data points in the distribution if we are referring to how we will apply this. A and B are the covariance matrices of their respective Gaussian probability functions (G_p). If one chooses an alpha value of 2, this conveniently allows us to take advantage of this property, for example, if we can define

$$\begin{aligned} P_{12} &= P_{21} \\ &= \int_{\mathfrak{R}} P_1(J, \Omega_-) P_2(J, \Omega_+) dJ \\ &= \frac{1}{n_1n_2} \sum_{i=1}^{n_1} \sum_{j=1}^{n_2} \int_{\mathfrak{R}} K_{\psi_1}(J - J(x_i)) \\ & \quad \times K_{\psi_2}(J - J(x_j)) dJ \\ &= \frac{1}{n_1n_2} \sum_{i=1}^{n_1} \sum_{j=1}^{n_2} (2\pi)^{-p/2} |\psi_1 + \psi_2|^{-1/2} \\ & \quad \times \exp\left(-\frac{1}{2}(J(x_i) - J(x_j))^T [\psi_1 + \psi_2]^{-1} \right. \\ & \quad \left. \times (J(x_i) - J(x_j))\right) \end{aligned} \quad (A2)$$

and similarly

$$P_{11} = \frac{1}{n_1n_1} \sum_{i=1}^{n_1} \sum_{i'=1}^{n_1} K_{2\psi_1}(J(x_i) - J(x_{i'})). \quad (A3)$$

We can also define

$$\begin{aligned} \hat{P}_{12}(J, \Omega) &= \int_{\mathfrak{R}} P_1(J, \Omega) K_{\psi_2}(J(C) - J) dJ \\ &= \frac{1}{n_1} \sum_{i=1}^{n_1} (2\pi)^{-p/2} |\psi_1 + \psi_2|^{-1/2} \\ & \quad \times \exp\left(-\frac{1}{2}(J(x_i) - J(C))^T [\psi_1 + \psi_2]^{-1} \right. \\ & \quad \left. \times (J(x_i) - J(C))\right) \end{aligned} \quad (A4)$$

and using these definitions we can rewrite Eq. (9) as

This simplification means the processing time of the algorithm increases as $O(pn^\alpha)$ where p is the number of input images and n is the number of samples used to estimate P_1 and P_2 . This is opposed to an increase of $O(n^p)$ which allows the consideration of a larger number of image features/modalities when segmenting. In the general case that alpha is an integer greater than 2, the property of Eq. (A2) can be applied recursively, for example, in the case of the integral of the product of n Gaussian functions

$$\begin{aligned} & \left(\prod_{i=1}^n \sum_{k^i=1}^s \right) \int_{\mathfrak{R}} \prod_{i=1}^n \frac{1}{|\Omega_i|} K_{\sigma_i} (J - J(x_{k^i})) \\ &= \left(\prod_{i=1}^n \sum_{k^i=1}^s \right) \frac{1}{(2\pi)^{p/2} \left(\prod_{i=1}^n |\psi_i|^{1/2} \right) \left| \left(\sum_{i=1}^n \psi_i^{-1} \right) \right|^{1/2}} \times \exp \left(-\frac{1}{2} \sum_{i=1}^{n-1} (d_i - x_{k^i})^T D_i (d_i - J(x_{k^i})) \right), \\ & \text{where } D_i = \left(\sum_{j=1}^{i+1} \psi_{kj}^{-1} \right)^{-1} \text{ and } d_i = \frac{\sum_{j=1}^i \psi_j x_{kj}}{\sum_{j=1}^i \psi_j}, \end{aligned} \tag{A6}$$

where s is the total number of samples taken from inside and outside the segment and k^i is the k th sample of the i th summation. To similarly reduce the number of integrals let us define the following terms:

$$\begin{aligned} \check{P}_{11} &= \alpha \int_{\mathfrak{R}} (w_1 P_1 (J, \Omega_-) + w_2 P_2 (J, \Omega_+))^{\alpha-1} \times (w_1 (k_{\sigma_1} (J(C) - J))) dJ \\ &= \alpha \int_{\mathfrak{R}} \sum_{l=0}^{\alpha-1} \binom{\alpha-1}{l} (w_1 P_1 (J, \Omega_-))^{\alpha-1-l} \times (w_2 P_2 (J, \Omega_+))^l w_1 (k_{\sigma_1} (J(C) - J)) dJ \\ &= \alpha \sum_{l=0}^{\alpha-1} \binom{\alpha-1}{l} \hat{\beta}_{11} w_1^{\alpha-l} w_2^l \frac{1}{(2\pi)^{p/2} (|\psi_1|^{\alpha-l} |\psi_2|^l |((\alpha-l)\psi_1^{-1} + l\psi_2^{-1})|)^{1/2}} \exp \left(-\frac{1}{2} \sum_{j=1}^{\alpha} (d_j - x_{k^j})^T D_j (d_j - x_{k^j}) \right), \\ & \text{where } x_{k^j} \in \Omega_- \text{ for } j = 1, 2 \dots \alpha - l, \\ & x_{k^j} \in \Omega_+ \text{ for } j = \alpha - l + 1, \dots \alpha - 1, \\ & x_{k^j} = J(C) \text{ iff } j = \alpha \\ & \text{and } \hat{\beta}_{11} = \frac{1}{n_1^{\alpha-l}} \left(\sum_{k^0=1}^{n_1} \sum_{k^1=1}^{n_1} \dots \sum_{k^{\alpha-l}=1}^{n_1} \right) \times \frac{1}{n_2^l} \left(\sum_{k^{0'}=1}^{n_2} \sum_{k^{1'}=1}^{n_2} \dots \sum_{k^{l'}=1}^{n_2} \right), \end{aligned} \tag{A7}$$

$$\begin{aligned} \bar{P}_{11} &= \alpha \int_{\mathfrak{R}} \left(\sum_{l=0}^{\alpha-1} \binom{\alpha-1}{l} \right) (w_1 P_1 (J, \Omega_-))^{\alpha-l} (w_2 P_2 (J, \Omega_+))^l dJ \\ &= -\alpha \sum_{l=0}^{\alpha-1} \binom{\alpha-1}{l} \beta_{11} w_1^{\alpha-l} w_2^l \frac{1}{(2\pi)^{p/2} (|\psi_1|^{\alpha-l} |\psi_2|^l |((\alpha-l)\psi_1^{-1} + l\psi_2^{-1})|)^{1/2}} \\ & \times \exp \left(-\frac{1}{2} \sum_{j=1}^{\alpha} (d_j - x_{k^j})^T D_j (d_j - x_{k^j}) \right), \\ & \text{where } x_{k^j} \in \Omega_- \text{ for } j = 1, 2 \dots \alpha - l + 1, \\ & x_{k^j} \in \Omega_+ \text{ for } j = \alpha - l + 2, \dots \alpha \\ & \text{and } \beta_{11} = \frac{1}{n_1^{\alpha-l+1}} \left(\sum_{k^0=1}^{n_1} \sum_{k^1=1}^{n_1} \dots \sum_{k^{\alpha-l+1}=1}^{n_1} \right) \times \frac{1}{n_2^l} \left(\sum_{k^{0'}=1}^{n_2} \sum_{k^{1'}=1}^{n_2} \dots \sum_{k^{l'}=1}^{n_2} \right). \end{aligned} \tag{A8}$$

Here the summations with a k^n and $k^{n'}$ refer to summations of the sample sets from inside and outside the segment. For completeness,

$$\begin{aligned} \check{P}_{22} &= \alpha \int_{\mathfrak{R}} (w_1 P_1(J, \Omega_-) + w_2 P_2(J, \Omega_+))^{\alpha-1} w_2 k_{\sigma_2}(J(C) - J) dJ \\ &= \alpha \int_{\mathfrak{R}} \sum_{l=0}^{\alpha-1} \binom{\alpha-1}{l} (w_1 P_1(J, \Omega_-))^{\alpha-1-l} \times (w_2 P_2(J, \Omega_+))^l w_2 (k_{\sigma_2}(J(C) - J)) dJ \\ &= \alpha \sum_{l=0}^{\alpha-1} \binom{\alpha-1}{l} \hat{\beta}_{22} w_1^{\alpha-1-l} w_2^{l+1} \frac{1}{(2\pi)^{p/2} (|\psi_1|^{\alpha-1-l} |\psi_2|^{l+1} |((\alpha-1-l)\psi_1^{-1} + (l+1)\psi_2^{-1})|)^{1/2}} \\ &\quad \times \exp\left(-\frac{1}{2} \sum_{j=1}^{\alpha} (d_j - x_{kj})^T D_j (d_j - x_{kj})\right), \end{aligned}$$

where $x_{kj} \in \Omega_-$ for $j = 1, 2, \dots, \alpha - 1 - l$,

$x_{kj} \in \Omega_+$ for $j = \alpha - l, \dots, \alpha - 1$,

$x_{kj} = J(C)$ iff $j = \alpha$

$$\text{and } \hat{\beta}_{22} = \frac{1}{n_1^{\alpha-1-l}} \left(\sum_{k^0=1}^{n_1} \sum_{k^1=1}^{n_1} \dots \sum_{k^{\alpha-1-l}=1}^{n_1} \right) \times \frac{1}{n_2^l} \left(\sum_{k^{0'}=1}^{n_2} \sum_{k^{1'}=1}^{n_2} \dots \sum_{k^{l'}=1}^{n_2} \right), \tag{A9}$$

$$\begin{aligned} \bar{P}_{22} &= \alpha \int_{\mathfrak{R}} \left(\sum_{l=0}^{\alpha-1} \binom{\alpha-1}{l} \right) (w_1 P_1(J, \Omega_-))^{\alpha-1-l} (w_2 P_2(J, \Omega_+))^{l+1} dJ \\ &= -\alpha \sum_{l=0}^{\alpha-1} \binom{\alpha-1}{l} \beta_{22} w_1^{\alpha-1-l} w_2^{l+1} \\ &\quad \times \frac{1}{(2\pi)^{p/2} (|\psi_1|^{\alpha-1-l} |\psi_2|^{l+1} |((\alpha-1-l)\psi_1^{-1} + (l+1)\psi_2^{-1})|)^{1/2}} \\ &\quad \times \exp\left(-\frac{1}{2} \sum_{j=1}^{\alpha} (d_j - x_{kj})^T D_j (d_j - x_{kj})\right), \end{aligned}$$

where $x_{kj} \in \Omega_-$ for $j = 1, 2, \dots, \alpha - l$,

$x_{kj} \in \Omega_+$ for $j = \alpha - l + 1, \dots, \alpha$

$$\text{and } \beta_{22} = \frac{1}{n_1^{\alpha-l}} \left(\sum_{k^0=1}^{n_1} \sum_{k^1=1}^{n_1} \dots \sum_{k^{\alpha-l}=1}^{n_1} \right) \times \frac{1}{n_2^{l+1}} \left(\sum_{k^{0'}=1}^{n_2} \sum_{k^{1'}=1}^{n_2} \dots \sum_{k^{(l+1)'}=1}^{n_2} \right), \tag{A10}$$

$$\begin{aligned} \bar{P}_{312} &= \int_{\mathfrak{R}} (w_1 P_1(J, \Omega_-) + w_2 P_2(J, \Omega_+))^\alpha dJ \\ &= \sum_{l=0}^{\alpha} \binom{\alpha}{l} \beta_3 w_1^{\alpha-l} w_2^l \frac{1}{(2\pi)^{p/2} (|\psi_1|^{\alpha-l} |\psi_2|^l |((\alpha-l)\psi_1^{-1} + (l)\psi_2^{-1})|)^{1/2}} \exp\left(-\frac{1}{2} \sum_{j=1}^{\alpha} (d_j - x_{kj})^T D_j (d_j - x_{kj})\right), \end{aligned}$$

where $x_{kj} \in \Omega_-$ for $j = 1, 2, \dots, \alpha - l$,

$x_{kj} \in \Omega_+$ for $j = \alpha - l + 1, \dots, \alpha$

$$\text{and } \beta_3 = \frac{1}{n_1^{\alpha-l}} \left(\sum_{k^0=1}^{n_1} \sum_{k^1=1}^{n_1} \dots \sum_{k^{\alpha-l}=1}^{n_1} \right) \times \frac{1}{n_2^l} \left(\sum_{k^{0'}=1}^{n_2} \sum_{k^{1'}=1}^{n_2} \dots \sum_{k^{l'}=1}^{n_2} \right), \tag{A11}$$

$$\begin{aligned}\check{P}_{31} &= \int_{\mathfrak{R}} P_1(J, \Omega)^{\alpha-1} k_{\sigma_1}(J(C) - J) dJ \\ &= \frac{1}{n_1^{\alpha-1}} \left(\sum_{k^1=1}^{n_1} \sum_{k^2=1}^{n_1} \cdots \sum_{k^{\alpha-1}=1}^{n_1} \right) \frac{1}{(2\pi)^{p/2} (\alpha |\psi_1|)^{1/2}} \times \exp \left(-\frac{1}{2} \sum_{j=1}^{\alpha} (d_j - x_{kj})^T D_j (d_j - x_{kj}) \right), \\ &\text{where } x_{kj} \in \Omega_- \text{ for } j = 1, 2, \dots, \alpha - 1 \\ &x_{kj} = J(C) \text{ iff } j = \alpha,\end{aligned}\tag{A12}$$

$$\begin{aligned}\check{P}_1 &= \int_{\mathfrak{R}} P_1(J(x), \Omega)^{\alpha} dx \\ &= \frac{1}{n_1^{\alpha}} \left(\sum_{k^0=1}^{n_1} \sum_{k^1=1}^{n_1} \cdots \sum_{k^{\alpha}=1}^{n_1} \right) \frac{1}{(2\pi)^{p/2} (\alpha |\psi_1|)^{1/2}} \times \exp \left(-\frac{1}{2} \sum_{j=1}^{\alpha} (d_j - x_{kj})^T D_j (d_j - x_{kj}) \right), \\ &\text{where } x_{kj} \in \Omega_- \text{ for all } j\end{aligned}\tag{A13}$$

\check{P}_2 and \check{P}_{32} are equivalent to \check{P}_1 and \check{P}_{31} , under the condition that P_2 , n_2 , and Ω_+ are substituted for P_1 , n_1 , and Ω_- . Considering these definitions, Eq. (9) can be rewritten as

$$\begin{aligned}\frac{\partial E(\phi)}{\partial t} &= \frac{1}{1-\alpha} \frac{\check{P}_{11} + \bar{P}_{11} + \check{P}_{22} + \bar{P}_{22}}{\bar{P}_{312}} \\ &+ \frac{\alpha}{1-\alpha} w_1 \frac{\check{P}_{31} + \check{P}_1}{\check{P}_1} - \frac{\alpha}{1-\alpha} w_2 \frac{\check{P}_2 - \check{P}_{32}}{\check{P}_2}.\end{aligned}\tag{A14}$$

^{a)} Author to whom correspondence should be addressed. Electronic mail: daniel.markel@mail.mcgill.ca

- ¹E. C. Halperin, C. A. Perez, and L. W. Brady, *Perez and Brady's Principles and Practice of Radiation Oncology* (Kluwer/Lippincott Williams & Wilkins, Philadelphia, PA, 2008).
- ²J. V. D. Steene, N. Linthout, J. D. Mey, V. Vinh-Hung, C. Claassens, M. Noppen, A. Bel, and G. Storme, "Definition of gross tumor volume in lung cancer: Interobserver variability," *Radiother. Oncol.* **62**, 37–49 (2002).
- ³S. Senan, J. van Sörnsen de Koste, M. Samson, H. Tankink, P. Jansen, P. J. Nowak, A. D. Krol, P. Schmitz, and F. J. Lagerwaard, "Evaluation of a target contouring protocol for 3D conformal radiotherapy in non-small cell lung cancer," *Radiother. Oncol.* **53**, 247–255 (1999).
- ⁴K. Mah, C. B. Caldwell, Y. C. Ung, C. E. Danjoux, J. M. Balogh, S. N. Ganguli, L. E. Ehrlich, and R. Tirona, "The impact of (18)FDG-PET on target and critical organs in CT-based treatment planning of patients with poorly defined non-small-cell lung carcinoma: A prospective study," *Int. J. Radiat. Oncol., Biol., Phys.* **52**, 339–350 (2002).
- ⁵J. J. Erasmus, G. W. Gladish, L. Broemeling, B. S. Sabloff, M. T. Truong, R. S. Herbst, and R. F. Munden, "Interobserver and intraobserver variability in measurement of nonsmall-cell carcinoma lung lesions: Implications for assessment of tumor response," *J. Clin. Oncol.* **21**, 2574–2582 (2003).
- ⁶P. A. Kupelian, C. Ramsey, S. L. Meeks, T. R. Willoughby, A. Forbes, T. H. Wagner, and K. M. Langen, "Serial megavoltage {CT} imaging during external beam radiotherapy for non-small-cell lung cancer: Observations on tumor regression during treatment," *Int. J. Radiat. Oncol., Biol., Phys.* **63**, 1024–1028 (2005).
- ⁷J. L. Barker, Jr., A. S. Garden, K. K. Ang, J. C. O'Daniel, H. Wang, L. E. Court, W. H. Morrison, D. I. Rosenthal, K. S. C. Chao, S. L. Tucker, R. Mohan, and L. Dong, "Quantification of volumetric and geometric changes occurring during fractionated radiotherapy for head-and-neck cancer using an integrated CT/linear accelerator system," *Int. J. Radiat. Oncol., Biol., Phys.* **59**, 960–970 (2004).

cer using an integrated CT/linear accelerator system," *Int. J. Radiat. Oncol., Biol., Phys.* **59**, 960–970 (2004).

- ⁸L. Xing, J. Seibers, and P. Keall, "Computational challenges for image-guided radiation therapy: Framework and current research," *Semin. Radiat. Oncol.* **17**, 245–257 (2007).
- ⁹J. Bradley, W. L. Thorstad, S. Mutic, T. R. Miller, F. Dehdashti, B. A. Siegel, W. Bosch, and R. J. Bertrand, "Impact of FDG-PET on radiation therapy volume delineation in non-small-cell lung cancer," *Int. J. Radiat. Oncol., Biol., Phys.* **59**, 78–86 (2004).
- ¹⁰A. C. Paulino, M. Koshy, R. Howell, D. Schuster, and L. W. Davis, "Comparison of CT- and FDG-PET-defined gross tumor volume in intensity-modulated radiotherapy for head-and-neck cancer," *Int. J. Radiat. Oncol., Biol., Phys.* **61**, 1385–1392 (2005).
- ¹¹U. Nestle, K. Walter, S. Schmidt, N. Licht, C. Neider, B. Motaref, D. Hellwig, M. Niewald, D. Ukena, C. M. Kirsch, G. W. Sybrecht, and K. Schnabel, "¹⁸F-Deoxyglucose positron emission tomography (FDG-PET) for the planning of radiotherapy in lung cancer: High impact in patients with atelectasis," *Int. J. Radiat. Oncol., Biol., Phys.* **44**, 593–597 (1999).
- ¹²P. Giraud, D. Grahek, F. Montravers, M. F. Carette, E. Deniaud-Alexandre, F. Julia, J. C. Rosenwald, J. M. Cosset, J. N. Talbot, M. Housset, and E. Touboul, "CT and ¹⁸F-deoxyglucose (FDG) image fusion for optimization of conformal radiotherapy of lung cancers," *Int. J. Radiat. Oncol., Biol., Phys.* **49**, 1249–1257 (2001).
- ¹³U. Nestle, S. Kremp, A. Schaefer-Schuler, C. Sebastian-Welsch, D. Hellwig, C. Rube, and C. M. Kirsch, "Comparison of different methods for delineation of ¹⁸F-FDG PET-positive tissue for target volume definition in radiotherapy of patients with non-small cell lung cancer," *J. Nucl. Med.* **46**, 1342–1348 (2005).
- ¹⁴A. C. Paulino and P. A. Johnstone, "FDG-PET in radiotherapy treatment planning: Pandora's box?" *Int. J. Radiat. Oncol., Biol., Phys.* **59**, 4–5 (2004).
- ¹⁵Q. C. Black, I. S. Grills, L. L. Kestin, C. Y. Wong, J. W. Wong, A. A. Martinez, and D. Yan, "Defining a radiotherapy target with positron emission tomography," *Int. J. Radiat. Oncol., Biol., Phys.* **60**, 1272–1282 (2004).
- ¹⁶K. J. Biehl, F. M. Kong, F. Dehdashti, J. Y. Jin, S. Mutic, I. El Naqa, B. A. Siegel, and J. D. Bradley, "¹⁸F-FDG PET definition of gross tumor volume for radiotherapy of non-small cell lung cancer: Is a single standardized uptake value threshold approach appropriate?" *J. Nucl. Med.* **47**, 1808–1812 (2006).
- ¹⁷A. van Baardwijk, G. Bosmans, L. Boersma, J. Buijsen, S. Wanders, M. Hochstenbag, R. J. V. Suylen, A. Dekker, C. Dehing-Oberije, R. Houben, S. M. Bentzen, M. V. Kroonenburgh, P. Lambin, and D. de Ruyscher, "PET-CT-based auto-contouring in non-small-cell lung cancer correlates with pathology and reduces interobserver variability in the

- delineation of the primary tumor and involved nodal volumes," *Int. J. Radiat. Oncol., Biol., Phys.* **68**, 771–778 (2007).
- ¹⁸D. A. Schinagl, W. V. Vogel, A. L. Hoffmann, J. A. V. Dalen, W. J. Oyen, and J. H. Kaanders, "Comparison of five segmentation tools for 18F-fluorodeoxy-glucose-positron emission tomography-based target volume definition in head and neck cancer," *Int. J. Radiat. Oncol., Biol., Phys.* **69**, 1282–1289 (2007).
- ¹⁹M. Hatt, F. Lamare, N. Bousson, A. Turzo, C. Collet, F. Salzenstein, C. Roux, K. Carson, P. Jarritt, C. C.-L. Rest, and D. Visvikis, "Fuzzy hidden Markov chains segmentation for volume determination and quantitation in PET," *Phys. Med. Biol.* **52**, 3467–3491 (2007).
- ²⁰D. W. G. Montgomery, A. Amira, and H. Zaidi, "Fully automated segmentation of oncological PET volumes using a combined multiscale and statistical model," *Med. Phys.* **34**, 722–724 (2007).
- ²¹D. L. Pham and J. L. Prince, "An adaptive fuzzy c-means algorithm for image segmentation in the presence of intensity inhomogeneities," *Pattern Recog. Lett.* **20**, 57–68 (1999).
- ²²J. C. Bezdek, L. O. Hall, M. C. Clark, D. B. Goldgof, and L. P. Clarke, "Medical image analysis with fuzzy models," *Stat. Methods Med. Res.* **6**, 191–214 (1997).
- ²³S. Belhassen and H. Zaidi, "A novel fuzzy C-means algorithm for unsupervised heterogeneous tumor quantification in PET," *Med. Phys.* **37**, 1309–1324 (2010).
- ²⁴Varian Medical Systems, "Eclipse: Treatment Planning System," Promotional brochure, 2013, Last accessed May 2nd, 2013 [available URL: <http://www.varian.com/media/oncology/products/eclipse/pdf/EclipseBrochure.pdf>].
- ²⁵A. Lin, G. Kubicek, J. W. Piper, A. S. Nelson, A. P. Dicker, and R. K. Valicenti, "Atlas-based segmentation in prostate IMRT: Timesavings in the clinical workflow," *Int. J. Radiat. Oncol., Biol., Phys.* **72**, S328–S329 (2008).
- ²⁶H. Zaidi and I. El Naqa, "PET-guided delineation of radiation therapy treatment volumes: A survey of image segmentation techniques," *Eur. J. Nucl. Med.* **37**, 2165–2187 (2010).
- ²⁷T. Sheperd, M. Teras, R. R. Beichel, R. Boellard, M. Bruynooghe, V. Dicken, M. J. Gooding, P. J. Julyan, J. A. Lee, S. Lefevre, M. Mix, V. Naranjo, X. Wu, H. Zaidi, Z. Zeng, and H. Minn, "Comparative study with new accuracy metrics or target volume contouring in PET image guided radiation therapy," *IEEE Trans. Med. Imaging* **31**, 2006–2024 (2012).
- ²⁸C. Xu and J. Prince, "Snakes, shapes, and gradient vector flow," *IEEE Trans. Image Process.* **7**, 359–369 (1998).
- ²⁹S. Osher and J. Sethian, "Fronts propagating with curvature-dependent speed: Algorithms based on Hamilton-Jacobi formulation," *J. Comput. Phys.* **79**, 12–49 (1988).
- ³⁰I. El Naqa, D. Yang, A. Apte, D. Khullar, S. Mucic, J. Zheng, J. D. Bradley, P. Grigsby, and J. O. Deasy, "Concurrent multimodality image segmentation by active contours for radiotherapy treatment planning," *Med. Phys.* **34**, 4738–4749 (2007).
- ³¹S. Milker-Zabel, A. Z. du Bois, M. Henze, P. Huber, D. Schulz-Ertner, A. Hoess, U. Haberkorn, and J. Debus, "Improved target volume definition for fractionated stereotactic radiotherapy in patients with intracranial meningiomas by correlation of CT, MRI and [68Ga]-DOTATOC-PET," *Int. J. Radiat. Oncol., Biol., Phys.* **65**, 222–227 (2006).
- ³²C. C. Caldwell, K. Mah, Y. C. Ung, C. E. Danjoux, J. M. Balogh, S. Ganguli, and L. E. Ehrlich, "Observer variation in contouring gross tumor volume in patients with poorly defined non-small-cell lung tumors on CT: The impact of ¹⁸F-FDG-hybrid PET fusion," *Int. J. Radiat. Oncol., Biol., Phys.* **51**, 923–931 (2001).
- ³³C. Greco, K. Rosenzweig, G. L. Cascini, and O. Tamburrini, "Current status of PET/CT for tumour volume definition in radiotherapy treatment planning for non-small cell lung cancer (NSCLC)," *Lung Cancer* **57**, 125–134 (2007).
- ³⁴I. Avazpour, R. E. Roslan, P. Bayat, M. I. Saripan, A. J. Nordin, and R. S. A. R. Abdullah, "Segmenting CT images of Bronchogenic carcinoma with bone metastases using PET intensity markers approach," *Radiol. Oncol.* **43**, 180–186 (2009).
- ³⁵H. Yu, C. B. Caldwell, K. Mah, and D. Mozeg, "Coregistered FDG PET/CT-based textural characterization of head and neck cancer for radiation treatment planning," *IEEE Trans. Med. Imaging* **28**, 374–383 (2009).
- ³⁶D. Han, J. Bayouth, Q. Song, A. Taurani, M. Sonka, J. Buatti, and X. Wu, "Globally optimal tumor segmentation in PET-CT images: A graph-based co-segmentation method," *Inf. Process. Med. Imaging* **6801**, 245–256 (2011).
- ³⁷Q. Song, J. Bai, D. Han, S. Bhatia, W. Sun, J. Bayouth, J. Buatti, and X. Wu, "Optimal co-segmentation of tumor in PET-CT images with context information," *IEEE Trans. Med. Imaging* **32**, 1685–1697 (2013).
- ³⁸A. B. Hamza and H. Krim, "Image registration and segmentation by maximizing the Jensen-Renyi divergence," *Lect. Notes Comput. Sci.* **2683**, 147–163 (2003).
- ³⁹F. Wang, T. Syeda-Mahmood, B. V. ad D. Beymer, and A. Rangarajan, "Closed-form Jensen Renyi divergence for mixture of Gaussians and applications to group-wise shape registration," in *Proceedings of the Medical Image Computing and Computer-Assisted Intervention* (Springer-Verlag, Berlin, 2009), Vol. 12, pp. 648–655.
- ⁴⁰J. N. Kapur, P. K. Shao, and A. K. C. Wong, "A new method of gray level picture thresholding using the entropy of histogram," *Comput. Vis. Graph. Image Process.* **29**, 273–285 (1985).
- ⁴¹T. Pun, "A new method for gray-level picture thresholding using the entropy of the histogram," *Signal Process.* **2**, 223–237 (1980).
- ⁴²T. Pun, "Entropic thresholding, a new approach," *Comput. Graph. Image Process.* **16**, 210–239 (1981).
- ⁴³J. Kim, J. W. Fisher, A. Yezzi, M. Çetin, and A. S. Willsky, "A non-parametric statistical method for image segmentation using information theory and curve evolution," *IEEE Trans. Image Process.* **14**, 1486–1502 (2005).
- ⁴⁴W. M. Wells III, P. Viola, H. Atsumi, S. Nakajima, and R. Kikinis, "Multimodal volume registration by maximization of mutual information," *Med. Image Anal.* **1**, 35–51 (1996).
- ⁴⁵H. Zaidi, M. Abdoli, C. L. Fuentes, and I. El Naqa, "Comparative methods for PET image segmentation in pharyngolaryngeal squamous cell carcinoma," *Eur. J. Nucl. Med.* **39**, 881–891 (2012).
- ⁴⁶J. F. Daisne, T. Duprez, B. Weynand, M. Lonneux, M. Hamoir, H. Reyckler, and V. Grégoire, "Tumor volume in pharyngolaryngeal squamous cell carcinoma: Comparison at CT, MR imaging, and FDG PET and validation with surgical specimen," *Radiology* **233**, 93–100 (2004).
- ⁴⁷J. F. Daisne, M. Sibomana, A. Bol, G. Cosnard, M. Lonneux, and V. Grégoire, "Evaluation of a multimodality image (CT, MRI and PET) coregistration procedure on phantom and head and neck cancer patients: Accuracy reproducibility and consistency," *Radiother. Oncol.* **69**, 237–245 (2003).
- ⁴⁸M. C. Chiang, R. A. Dutton, K. M. Hayashi, A. W. Toga, O. L. Lopez, H. J. Aizenstein, J. T. Becker, and P. M. Thompson, "Fluid registration of medical images using Jensen-Renyi divergence reveals 3D profile of brain atrophy in HIV/AIDS," in *Proceedings of the IEEE International Symposium on Biomedical Imaging (ISBI2006)* (IEEE, Arlington, VA, 2006), pp. 193–196.